Polarized Optical-Flow Gyroscope

Masada Tzabari and Yoav Y. Schechner

Viterbi Faculty of Electrical Engineering,
Technion - Israel Institute of Technology Haifa 32000, Israel
masada.tz@campus.technion.ac.il ; yoav@ee.technion.ac.il
http://www.ee.technion.ac.il/~yoav

Abstract. We merge by generalization two principles of passive optical sensing of motion. One is common spatially resolved imaging, where motion induces temporal readout changes at high-contrast spatial features, as used in traditional optical-flow. The other is the polarization compass, where axial rotation induces temporal readout changes due to the change of incoming polarization angle, relative to the camera frame. The latter has traditionally been modeled for uniform objects. This merger generalizes the brightness constancy assumption and optical-flow, to handle polarization. It also generalizes the polarization compass concept to handle arbitrarily textured objects. This way, scene regions having partial polarization contribute to motion estimation, irrespective of their texture and non-uniformity. As an application, we derive and demonstrate passive sensing of differential ego-rotation around the camera optical axis.

Keywords: Low level vision, Self-calibration, Bio-inspired

1 Introduction

Spatio-temporal image intensity variations indicate motion by low-level vision. This is the *optical-flow* principle. Image-based sensing makes several assumptions. First, the object must have significant spatial contrast of intensity (see Fig. 1). If the scene is nearly uniform, motion estimation is ill-conditioned. Second, spatial resolution should be high, for better conditioning of motion sensing. Third, optical-flow is generally derived assuming *brightness constancy*, i.e, the radiance of observed features is time invariant. Moreover, consider sensing ego-rotation around the camera optical axis. The visual signal useful for this is at the periphery of the field of view. The closer pixels are to the image center (Fig. 1), the less they contribute to image-based sensing of ego-rotation. There, temporal differential variations of intensity tend to null.

There is another principle of passive optical sensing, which can be used for determining orientation and its change (rotation): *polarimetry*. Generally, light coming from a scene towards a sensor has partial linear polarization. The scene polarization is at some angle, set in the object coordinate system. This is the angle of polarization (AOP). Assume a polarization filter is mounted on an optical sensor. The filter has a lateral axis: light is maximally transmitted through

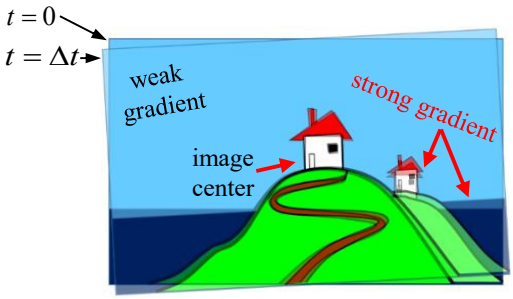

Fig. 1. Types of image regions that are friendly to either optical-flow or polarization-based estimation of rotation. A region of very weak spatial gradient is very suitable for polarization-based estimation. An off-center region of strong gradient is very suitable for optical flow estimation. In the central region of the image, intensity barely changes temporally, despite rotation. Therefore it is not informative in image-based estimation. It is, however, useful in a polarization compass.

the filter if the AOP is aligned with this filter. Multiple measurements by the sensor, in each of which the filter axis is different, can determine the AOP and thus the orientation of the sensing system relative to the object. This principle is known as a *polarization compass*. It is used by many animals [27, 82] which exploit celestial or underwater polarization for navigation.

Note that models of the polarization compass *do not use imaging*, i.e, spatial resolution is not required. Rather crude optical sensors having a broad field of view are used. Polarimetry relies on very different - even contradictory - assumptions, relative to image-based methods as optical-flow. Traditional polarimetry has thus far assumed point-wise analysis, oblivious to spatial gradients. *Rotation estimation using polarimetry thrives on spatially uniform objects*, as the sky. On the other hand, image-based methods thrive on high resolution sensing of scenes having high contrast spatial features.

This paper combines the two principles of *optical flow* and *polarization compass*. This enables estimation of motion, and particularly ego-rotation, using both uniform and high-contrast scene regions. Note that in a scene, most image regions have low contrast, and have thus far not been effective for motion estimation by optical-flow. By combining the polarization compass principle with optical flow, partially-polarized areas can help in motion assessments even if they have low contrast, while high-contrast image regions can help as in optical-flow.

On one hand, we generalize *brightness constancy* and *optical-flow* to polarization signals. On the other hand, we generalize the concept of *polarization compass* to spatially-varying signals of arbitrary contrast. Consequently, the paper formulates models and inverse problems that rely on these generalizations. We demonstrate a solution both in simulations and real experiments. We assume polarization-constancy. When does it hold? A major motivation is polarization compass using atmosphere or underwater ambient scattered light [17, 18, 19, 21, 67, 79]. In both domains, polarization constancy holds and is in-

variant to translation. However, when polarization is created by reflection and refraction, it can strongly vary with the direction an object is observed from. There, if translational motion changes the viewpoint significantly, our assumption becomes invalid. The assumption would still hold when the reflective scene is distant relative to lateral translation.

2 Prior Work

Polarization is used by a wide range of animals [13, 63, 64, 65, 66, 67], particularly for navigation [7, 8, 20, 24, 47, 82]. Notable animals in this context are bees, ants, squid, spiders, locust, migratory birds, butterflies, crab and octopus. Some of these animals have very crude spatial resolution and most of them have very small brains. In other words, their vision resources are limited. However, observing the sky polarization, even in poor resolution, yields a strong navigational cue which requires minimal computational resources (low level).

Polarization compass is used in bio-inspired robot navigation [17, 18, 19, 21, 69, 81], relying mainly on celestial or underwater polarization patterns. These robotic systems therefore can use low resources, and reduce dependency on GPS and inertial measurement units (IMUs). This is our inspiration as well. Low-resource approaches in computer vision [9, 12, 26, 32, 53, 72, 73, 75] are significant facilitators of small, distributed agents, using low power, narrow communication bandwidth, reduced computations and crude optical resolution.

Refs. [29, 30] use the degree of polarization (DOP), instead of radiance, as input to classic optical-flow. As in our work, [29, 30] assume polarization constancy. However, when only the DOP is the input to optical-flow, the formulation is insensitive to the incoming light's AOP, relative to the camera. Hence, the formulation is oblivious to the polarization-compass principle, which provides point-wise sensitivity to the camera orientation and its rotation rate. For example, in a scene having near-uniform DOP as the sky, the DOP does not indicate rotation. Our paper does *not substitute* radiance by DOP. Instead, we *generalize* optical flow to be sensitive to all components of the polarization vector field, and can estimate the rotation rate even from a single pixel.

We estimate the state of an imaging system by observing an unknown scene. This is related to self-calibration. Self-calibration in the context of polarization has been recently suggested [58, 85]. In [58], there is no motion of the camera or the object. Self calibration there applies to angles of a polarizer, using redundant images (multi-pixel images in four or more polarizer angles).

More broadly, several scientific communities rely on imaging polarization of light. Specifically, atmospheric sciences and astronomy rely on it [3, 16, 35, 40, 59, 79], to remotely-sense micro-physical properties of particles or separate scene components. In computational photography, polarization is used in a variety of imaging systems [5, 11, 14, 28, 36, 37, 48, 54, 56, 77, 83]. Polarization is helpful for solving a variety of inverse problems [57] in imaging. These include separation of reflection components and surface shape estimation [15, 22, 31, 34, 39, 41, 42, 45, 49, 51, 51, 80, 86], descattering [33, 43, 44, 74, 78], and physics-based rendering [11].

Polarization is also used in computational displays [4, 46, 52] and camera-based communication [84].

Optical-flow is another low-level vision method. As such, it is suitable for low-resource systems, e.g., when computing, power or lag-time constraints prohibit using higher-level processing such as structure-from-motion. It is also independent of external systems [62, 70]. Therefore, animals having small brains [71] seem to estimate ego-motion estimation using optical-flow. Similarly, optical-flow is used in airborne and land robots [2, 10, 23, 50, 55, 68, 71, 76].

3 Theoretical Background

3.1 Reference Frames and Polarization

An optical axis is perpendicular to a lateral plane. Three frames of reference are in the plane: the object, camera and polarizer frames. Coordinates $\boldsymbol{x}_{\rm cam} = [x_{\rm cam}, y_{\rm cam}]^\top$ in the camera frame express the pixel on the sensor array. Here $\top$ denotes transposition. The object frame is $\boldsymbol{x}_{\rm obj} = [x_{\rm obj}, y_{\rm obj}]^\top$, where $x_{\rm obj}$ and $y_{\rm obj}$ are lateral coordinates of the object. They are respectively referred to here as *horizontal* and *vertical* world coordinates. In the object coordinate frame, radiance from an object location is characterized by intensity $c(\boldsymbol{x}_{\rm obj})$, DOP $p(\boldsymbol{x}_{\rm obj})$, and AOP $\theta(\boldsymbol{x}_{\rm obj})$.

A polarization filter (analyzer) is mounted in front of the camera. The *polarizer axis* is the chief lateral direction in the filter frame. When light is incident at the filter, the polarization component parallel to the polarizer axis is transmitted. The polarization component perpendicular to the polarizer axis is blocked. The angle $\alpha^{\rm in}_{\rm pol}$ indicates azimuth of a vector, relative to the polarizer axis.

There are relations between the frames of reference. The polarizer axis is oriented at an angle α relative to the horizon in the object frame. A projection operator $\mathcal{T}$ relates the object and camera coordinates:

$$\boldsymbol{x}_{\rm cam} = \mathcal{T}\boldsymbol{x}_{\rm obj}. \tag{1}$$

Light from an object passes through the polarization filter, and then hits the camera sensor array. The measured intensity at the sensor pixel is then

$$I(\boldsymbol{x}_{\rm cam}) = I(\mathcal{T}\boldsymbol{x}_{\rm obj}) = \frac{c(\boldsymbol{x}_{\rm obj})}{2}\left\{1 + p(\boldsymbol{x}_{\rm obj})\cos 2\left[\alpha - \theta(\boldsymbol{x}_{\rm obj})\right]\right\}. \tag{2}$$

3.2 Traditional Optical-Flow

Traditional optical-flow assesses a velocity vector field $\boldsymbol{v}(\boldsymbol{x}_{\rm cam})$ in the camera plane. Traditionally, a polarization filter has not been part of the imaging optics in optical-flow formulations. In unpolarized (radiometric) imagery, the measured intensity at the detector is

$$I(\boldsymbol{x}_{\rm cam}) = I(\mathcal{T}\boldsymbol{x}_{\rm obj}) = c(\boldsymbol{x}_{\rm obj})\ . \tag{3}$$

Let t denote time. Optical-flow relies on *brightness constancy*: an object patch inherently has static, time invariant radiance:

$$\frac{dc(\boldsymbol{x}_{\rm obj})}{dt} = 0 \ . \tag{4}$$

Brightness constancy means that images vary in time only due to relative motion between the object coordinates and the camera coordinates. The motion affects the projection operator of Eq. (1). Locally, it is assumed that differential motion is rigid: after differential time dt, a spatial patch which was projected to $\boldsymbol{x}_{\rm cam}$ is shifted according to

$$\boldsymbol{x}_{\rm cam} \ \longrightarrow \ \ \boldsymbol{x}_{\rm cam} + \boldsymbol{v}(\boldsymbol{x}_{\rm cam})dt. \tag{5}$$

This shift induces a temporal differential change in the measured intensity at $\boldsymbol{x}_{\rm cam}$, satisfying

$$\frac{\partial I(\boldsymbol{x}_{\rm cam})}{\partial t} + \nabla I(\boldsymbol{x}_{\rm cam}) \cdot \boldsymbol{v}(\boldsymbol{x}_{\rm cam}) = 0. \tag{6}$$

Here ∇I is the spatial gradient field of the measured intensity. Note that Eq. (5) ignores local orientation changes, i.e. traditional methods assume that a local translation-only model may suffice. This assumption cannot hold when polarization is involved, because local orientation changes directly induce changes of measured intensity at the camera, as we discuss.

4 Polarized-Flow

We introduce polarized optical-flow. It generalizes several basic concepts.

- The optical-flow model (Eq. 6) is extended by generalizing brightness constancy (Eq. 4). The essence is extension of Eq. (5) to account for local orientation changes in the projected scene, relative to a camera-mounted polarization filter. This enables quantification of orientation changes even where $\nabla I(\boldsymbol{x}_{\rm cam}) = 0$.
- Polarization filtering can sense orientation, creating a *polarization compass*. It has so far been formulated for objects having spatially uniform radiance, e.g., zenith view of a clear sky. In polarized-flow, this compass is generalized to arbitrarily nonuniform scenes, where $\nabla I(\boldsymbol{x}_{\rm cam}) \neq 0$. This is done using a formulation of differential spatio-temporal changes of measured intensities.

A camera might sense all components of the polarization vector field, by having special pixel-based polarization filters [29,30]. We show that a much simpler sensor can be used: a uniform filter over the whole field of a standard camera. It suffices to obtain enhanced flow estimation and particularly the rotation rate, despite uncertain information about the object's Stokes vector. We use a camera which rigidly rotates in front of a static scene, as illustrated in Fig. 2.

4.1 Polarized Optical-Flow Equation

The transfer of coordinate systems $\mathcal{T}$ (Eq. 1) during projection changes any *orientation* associated with a local patch. Specifically, consider an object for which

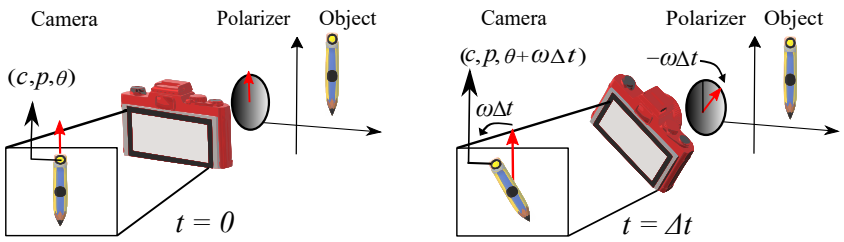

Fig. 2. The camera sensor and the polarizer reference frames are coupled. The coupled camera+polarizer system rotates around the optical axis, which is common to all three reference frames. Angular velocity is positive for counter-clockwise motion. Between shots, the rotation angle is $\omega\Delta t$. The AOP of the object, though static in the object frame, tilts by $\omega\Delta t$ relative to the polarizer axis.

the AOP $\theta(\boldsymbol{x}_{\rm obj})$ is uniform. In the camera coordinate system, the projection yields an AOP $\theta(\boldsymbol{x}_{\rm cam}) = \mathcal{T}\theta(\boldsymbol{x}_{\rm obj})$.

Now, let $\mathcal{T}$ change in time. The change in $\mathcal{T}$ involves rotation at rate $-\omega$ around the optical axis. Then, during an infinitesimal time of dt

$$\theta(\boldsymbol{x}_{\rm cam}) \;\longrightarrow\; \theta(\boldsymbol{x}_{\rm cam}) + \omega dt \; . \tag{7}$$

This relation holds when $\theta(\boldsymbol{x}_{\rm cam})$ is spatially uniform, or when viewing a static object on the optical axis. In the latter case, $\boldsymbol{v}(\boldsymbol{x}_{\rm cam}) = 0$ in Eq. (5).

Generally, there is change of orientation, lateral motion, and spatial non-uniformity. This compounds Eqs. (5,7):

$$\theta(\boldsymbol{x}_{\rm cam}) \;\longrightarrow\; \theta[\boldsymbol{x}_{\rm cam} + \boldsymbol{v}(\boldsymbol{x}_{\rm cam})dt] + \omega dt \; . \tag{8}$$

During differential time dt, assume that the inherent radiance of the object is static, in the object's own coordinate system. Then Eq. (4) generalizes to

$$\frac{dc(\boldsymbol{x}_{\rm obj})}{dt} = 0 \qquad \frac{dp(\boldsymbol{x}_{\rm obj})}{dt} = 0 \qquad \frac{d\theta(\boldsymbol{x}_{\rm obj})}{dt} = 0 \; . \tag{9}$$

In the camera coordinate system, Eq. (6) generalizes to

$$\begin{aligned}
&\frac{\partial c(\boldsymbol{x}_{\rm cam})}{\partial t} + \nabla c(\boldsymbol{x}_{\rm cam}) \cdot \boldsymbol{v}(\boldsymbol{x}_{\rm cam}) = 0 \\
&\frac{\partial p(\boldsymbol{x}_{\rm cam})}{\partial t} + \nabla p(\boldsymbol{x}_{\rm cam}) \cdot \boldsymbol{v}(\boldsymbol{x}_{\rm cam}) = 0 \\
&\frac{\partial \theta(\boldsymbol{x}_{\rm cam})}{\partial t} + \nabla \theta(\boldsymbol{x}_{\rm cam}) \cdot \boldsymbol{v}(\boldsymbol{x}_{\rm cam}) = \omega.
\end{aligned} \tag{10}$$

Note specifically how the presence of ω in Eq. (8) affects the orientation (last) relation in Eq. (10). Recall that a camera only measures raw intensity $I(\boldsymbol{x}_{\rm cam})$, rather than c, p, θ. The polarimetric and intensity variables relate through Eq. (2). Let us transfer Eq. (2) to explicit dependency on camera coordinates, in case

the *polarization filter is rigidly tied to the camera*. The camera coordinate system then dictates the polarizer coordinate system. If $\mathcal{T}$ involves rotation of the camera at rate $-\omega$ (in the object coordinate system), then the polarizer axis changes at rate $-\omega$ in the object coordinate system.

Prior to rotation, the angle between the object polarization and the polarizer axis is $[\alpha-\theta(\boldsymbol{x}_{\rm obj})]$. After time dt, this relative angle changes to $[\alpha+\omega dt-\theta(\boldsymbol{x}_{\rm obj})]$. Following Eq. (2), the change of the relative angle induces a temporal change in $I(\boldsymbol{x}_{\rm cam})$, even if c, p, θ are spatially uniform.

We now include both polarization-induced differential changes to $I(\boldsymbol{x}_{\rm cam})$, as well as changes to $I(\boldsymbol{x}_{\rm cam})$ created by motion as in common optical-flow. Without loss of generality, prior to rotation, let the polarizer axis be horizontal in the object coordinate system, i.e., $\alpha = 0$. Then,

$$\begin{aligned}
&\frac{\partial I(\boldsymbol{x}_{\rm cam})}{\partial t} + \nabla I(\boldsymbol{x}_{\rm cam}) \cdot \boldsymbol{v}(\boldsymbol{x}_{\rm cam}) = \\
&\quad \frac{1}{2}\frac{\partial c}{\partial t} + \frac{1}{2}\left\{ p\frac{\partial c}{\partial t} + c\frac{\partial p}{\partial t} \right\} \cos(2\theta) - cp\sin(2\theta)\frac{\partial \theta}{\partial t} + \\
&\quad \frac{1}{2}\frac{\partial c}{\partial x} + \frac{1}{2}\left\{ p\frac{\partial c}{\partial x} + c\frac{\partial p}{\partial x} \right\} \cos(2\theta) - cp\sin(2\theta)\frac{\partial \theta}{\partial x} + \\
&\quad \frac{1}{2}\frac{\partial c}{\partial y} + \frac{1}{2}\left\{ p\frac{\partial c}{\partial y} + c\frac{\partial p}{\partial y} \right\} \cos(2\theta) - cp\sin(2\theta)\frac{\partial \theta}{\partial y} = \\
&\frac{1+p\cos 2\theta}{2}\left\{ \frac{\partial c}{\partial t} + \nabla c \cdot \boldsymbol{v} \right\} + \frac{c\cos 2\theta}{2}\left\{ \frac{\partial p}{\partial t} + \nabla p \cdot \boldsymbol{v} \right\} - cp\sin 2\theta \left\{ \frac{\partial \theta}{\partial t} + \nabla \theta \cdot \boldsymbol{v} \right\}.
\end{aligned} \tag{11}$$

Using Eq. (10) in Eq. (11) yields the *polarized optical-flow equation*

$$\frac{\partial I(\boldsymbol{x}_{\rm cam})}{\partial t} + \nabla I(\boldsymbol{x}_{\rm cam}) \cdot \boldsymbol{v}(\boldsymbol{x}_{\rm cam}) + \omega c(\boldsymbol{x}_{\rm cam}) p(\boldsymbol{x}_{\rm cam}) \sin[2\theta(\boldsymbol{x}_{\rm cam})] = 0. \tag{12}$$

For the special case $p = 0$, Eq. (12) degenerates to the traditional optical-flow equation, as required. Moreover, because a change in θ is solely due to rotation of the camera+filter relative to the object, the special case $\omega = 0$ also degenerates Eq. (12) to the traditional optical-flow equation, irrespective of p. The model may be applied to ego-rotation sensing.

5 Quantifying Sensitivities

We want to assess the significance of the polarization-compass relative to image-based spatially resolving analysis of rotation. The image-based principle is analyzed using pairs of distinct pixels, say edge-lets. The polarimetric principle is analyzed using a broad uniform area in the field of view.

5.1 Image-Based Sensitivity

Let us start with the image-based principle. There are $N_{\rm cam}$ pixels in the camera. Between random pairs of edge-let pixels, a vector is typically of length $R \sim$

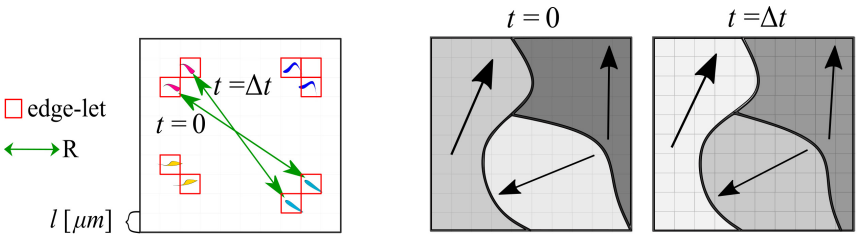

Fig. 3. [Left] The imager has N_{cam} pixels. A typical distance between edge-lets is $R \sim \sqrt{N_{\text{cam}}}/2$ pixels. Between frames, there is time step Δt and the image rotates. If edge-lets move by a pixel, their relative rotation is sensed. Each pixel is of length l microns. [Right] An object is divided to K segments (here K=3). Each segment has approximately uniform polarization (marked by an arrow). Due to slight rotation of a camera+polarizer rig, the measured intensity per segment changes slightly.

$\sqrt{N_{\text{cam}}}/2$ pixels (Fig.3 [Left]). Rotation means that the inter-pixel vector tilts slightly within a time step of Δt. A single pixel is the basic resolution of this vector tilt. Hence the edge-let pair can resolve a rotation rate $\Delta\omega_{\text{pair}}$ given by

$$\Delta\omega_{\text{pair}} \sim [\Delta t\sqrt{N_{\text{cam}}}/2]^{-1} , \tag{13}$$

irrespective of the pixel size. Let there be $N_{\text{edge-lets}}$ independent edge-lets, thus $\approx N^2_{\text{edge-lets}}$ pairs. Each of them contributes an independent random error of standard deviation $\Delta\omega_{\text{pair}}$ to the estimated rotation rate. Averaging the contributions, overall, an image-based method can resolve

$$\Delta\omega_{\text{image}} = \sqrt{\sum_{\text{pair}=1}^{N^2_{\text{edge-lets}}} \left(\frac{\Delta\omega_{\text{pair}}}{N^2_{\text{edge-lets}}}\right)^2} \sim [N_{\text{edge-lets}}\Delta t\sqrt{N_{\text{cam}}}/2]^{-1} . \tag{14}$$

5.2 Polarimetric sensitivity

Now, let us deal with polarimetry in a spatially uniform region (segment) (Fig.3 [Right]). Consider two rotation rates, whose difference is $\Delta\omega$. From Eq. (12), due to rotation during Δt, the intensity of a pixel changes temporally according to

$$\Delta I(\boldsymbol{x}_{\text{cam}}) = \Delta\omega\Delta t\ c(\boldsymbol{x}_{\text{cam}})p(\boldsymbol{x}_{\text{cam}})|\sin[2\theta(\boldsymbol{x}_{\text{cam}})]| . \tag{15}$$

For a random orientation $\theta(\boldsymbol{x}_{\text{cam}})$, let us set roughly $|\sin[2\theta(\boldsymbol{x}_{\text{cam}})]|\sim 1/2$. From Eq. (2), $I(\boldsymbol{x}_{\text{cam}}) \sim c(\boldsymbol{x}_{\text{cam}})/2$. Hence, due to the object segment, a resolvable orientation rate is roughly

$$\Delta\omega^{\text{segment}}_{\text{polar}} \sim 4\Delta I\,[Ip\Delta t]^{-1} , \tag{16}$$

where we drop the dependency on $\boldsymbol{x}_{\text{cam}}$ due to the uniformity of the segment. Here ΔI is the resolvable intensity, which is determined by radiometric noise.

When a camera is well exposed, noise is dominated by photon (Poisson) statistics. Thus $\Delta I \approx \sqrt{I}$, where I is in units of photo-electrons. The typical full-well depth of a pixel is $\sim 1000l^2$ photo-electrons, where l is the pixel width in microns (Fig.3 [left]). The object occupies $N_{\rm cam}/K$ pixels, where K is the number of image segments, each being uniform. The intensity over this area is aggregated digitally. This aggregation is equivalent to a full well of $\sim 1000N_{\rm cam}l^2/K$ photo-electrons per segment. Let the sensor be exposed at medium-level i.e., at half-well. Summing photo-electrons from all pixels in a segment, the signal and its uncertainty are, respectively,

$$I \approx 500N_{\rm cam}l^2/K \ , \quad \Delta I \approx \sqrt{500N_{\rm cam}l^2/K}. \tag{17}$$

Combining Eqs. (16,17)

$$\Delta\omega_{\rm polar}^{\rm segment} \sim 4\sqrt{K}\left[pl\Delta t\sqrt{500N_{\rm cam}}\right]^{-1} \ . \tag{18}$$

Averaging information from all K segments in the image, polarimetry can resolve

$$\Delta\omega_{\rm polar} = \sqrt{\sum_{\rm segment=1}^{K}\left(\frac{1}{K}\Delta\omega_{\rm polar}^{\rm segment}\right)^2} \sim 4\left[pl\Delta t\sqrt{500N_{\rm cam}}\right]^{-1} \ . \tag{19}$$

As expected, the uncertainty $\Delta\omega_{\rm polar}$ becomes smaller, as p or l increase. In other words the higher the object polarization or the better light gathering by the camera detector, the lower is the uncertainty. From Eqs. (14,19),

$$\Delta\omega_{\rm polar} \approx \frac{N_{\rm edge-lets}}{11pl}\Delta\omega_{\rm image} \ . \tag{20}$$

We examine this relation for a few case studies.
• If $l = 10\mu m$, $p = 0.5$, then the uncertainty ratio is $\approx N_{\text{edge-lets}}/56$. Hence, if there are about 50 reliable edge-lets in the image, polarization contributes similarly to image-based flow.
• If $l = 3\mu m$, $p = 0.05$, then the uncertainty ratio is $\approx N_{\text{edge-lets}}/1.7$. If as before there are 50 reliable edge-lets in the image, polarization barely contributes information, relative to image-based flow. Polarization contributes here significantly only if the image is extremely smooth, or comprises of very few pixels.
• For a single pixel sensor (or pair of pixels) the uncertainty ratio is $\approx (11pl)^{-1}$, suggesting high potential to polarization contribution. In this case, spatial non-uniformity would have no impact. The mean intensity of an image may be considered equivalent to a single pixel approximation. A constant rotation rate may be estimated by fitting the change in the mean intensity of the image due to rotation to Eq. (2). This would require a sequence of images from four time steps (see examples in *Supplementary Material*).

The study cases above demonstrate polarization has the best added value for scenes having high polarization, few spatial features, and cameras having low-resolution, or large pixels and hence high SNR.

6 Polarized-Flow Gyro Forward Model

Let us now analyze the case of pure rotational motion around the optical center of the rig (camera + polarizing filter), as in Fig. 2. In the coupled frame, the image rotates with angular velocity of ω, around a center pixel $\overline{\boldsymbol{x}}_{\rm cam}$. Moreover, let the object be static. Then, in the camera reference frame,

$$\boldsymbol{v} = [-\omega(y_{\rm cam} - \overline{y}_{\rm cam}),\ \omega(x_{\rm cam} - \overline{x}_{\rm cam})]. \tag{21}$$

Define $\Gamma(\boldsymbol{x}_{\rm cam}) = c(\boldsymbol{x}_{\rm cam})p(\boldsymbol{x}_{\rm cam})\sin 2\theta(\boldsymbol{x}_{\rm cam})$ and $b(\boldsymbol{x}_{\rm cam}) = \frac{\partial I(\boldsymbol{x}_{\rm cam})}{\partial t}$. From Eqs. (12,21),

$$\omega(y_{\rm cam} - \overline{y}_{\rm cam})\frac{\partial I(\boldsymbol{x}_{\rm cam})}{\partial x_{\rm cam}} - \omega(x_{\rm cam} - \overline{x}_{\rm cam})\frac{\partial I(\boldsymbol{x}_{\rm cam})}{\partial y_{\rm cam}} - \omega\Gamma(\boldsymbol{x}_{\rm cam}) = b(\boldsymbol{x}_{\rm cam}). \tag{22}$$

Define

$$q(\boldsymbol{x}_{\rm cam}) = \frac{\partial I(\boldsymbol{x}_{\rm cam})}{\partial x_{\rm cam}}(y_{\rm cam} - \overline{y}_{\rm cam}) - \frac{\partial I(\boldsymbol{x}_{\rm cam})}{\partial y_{\rm cam}}(x_{\rm cam} - \overline{x}_{\rm cam}) - \Gamma(\boldsymbol{x}_{\rm cam}). \tag{23}$$

Then, per pixel $\boldsymbol{x}_{\rm cam}$, Eqs. (12,22) can be expressed as $b(\boldsymbol{x}_{\rm cam}) - q(\boldsymbol{x}_{\rm cam})\omega = 0$. For N pixels, define the vectors $\boldsymbol{q} = [q(\boldsymbol{x}_{{\rm cam}_1}), q(\boldsymbol{x}_{{\rm cam}_2}), \ldots, q(\boldsymbol{x}_{{\rm cam}_N})]^\top$ and $\boldsymbol{b} = [b(\boldsymbol{x}_{{\rm cam}_1}), b(\boldsymbol{x}_{{\rm cam}_2}), \ldots, b(\boldsymbol{x}_{{\rm cam}_N})]^\top$. Then,

$$\boldsymbol{q}\omega = \boldsymbol{b}. \tag{24}$$

7 Solving a Polarized-Flow Gyro Inverse Problem

We now estimate the angular velocity ω. Assume for the moment that vectors $\boldsymbol{q}$ and $\boldsymbol{b}$ are known. Note that Eq. (24) is a set of linear equations with a single unknown. A least-squares solution is given in closed-form:

$$\hat{\omega} = (\boldsymbol{q}^\top \boldsymbol{q})^{-1}\boldsymbol{q}^\top \boldsymbol{b}. \tag{25}$$

Let ω be known, but c, p and θ be unknown. Eq. (22) is sensitive only to the vector $\boldsymbol{\Gamma} = [\Gamma(\boldsymbol{x}_{{\rm cam}_1}), \Gamma(\boldsymbol{x}_{{\rm cam}_2}), \ldots, \Gamma(\boldsymbol{x}_{{\rm cam}_N})]^\top$. Let us estimate it by

$$\hat{\boldsymbol{\Gamma}} = \arg\min_{\boldsymbol{\Gamma}} \left[\sum_{\boldsymbol{x}_{\rm cam}} \left| b(\boldsymbol{x}_{\rm cam}) - q(\boldsymbol{x}_{\rm cam})\omega \right|^2 + \mu \|\nabla^2 \boldsymbol{\Gamma}\|_2^2 \right], \tag{26}$$

where μ is a regularization weight. Eq. (26) is quadratic in Γ, and thus has a closed-form solution. It can be applied when analyzing small images. For high-resolution images, Eq. (26) is solved iteratively by gradient descent.

Eq. (26) assumes that ω is known, while Eq. (25) assumes that $\boldsymbol{\Gamma}$ is known. We alternate between these two processes, starting from an initial $\hat{\omega}$. In our implementation, we ran 50 iterations of Eq. (26) between each calculation of Eq. (25), and repeated to convergence. Note that for the application of ego-rotation estimation, our main interest is estimation of $\hat{\omega}$. The estimation of $\hat{\boldsymbol{\Gamma}}$ is a means to that end, hence we tolerate errors in $\hat{\boldsymbol{\Gamma}}$.

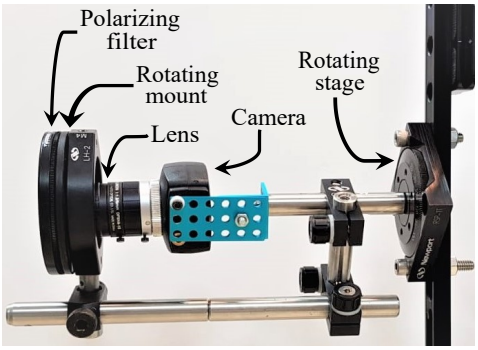

Fig. 4. The coupled camera-polarizer system for simulation and experiments. The polarizer is harnessed to the camera on a rotating mount, allowing measurements of the Stokes vector. The system is assembled on a tripod for stability.

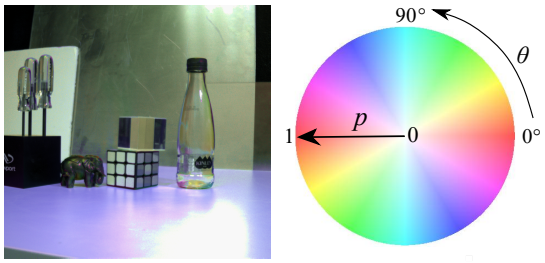

Fig. 5. [Left] Scene used in the simulation, visualized in color using the HSV space. Gamma correction of the intensity was performed for display purposes. [Right] The HSV coordinates are θ (Hue), p (Saturation), and c (Value).

8 Simulation Based on Real Data

Before conducting real experiments, we performed simulations using images $I(\boldsymbol{x}_{\text{cam}}, t)$ rendered from real polarimetry. To acquire data, we used a setup shown in Fig. 4. An IDS 4.92 megapixel monochrome camera (UI-3480LE) was fitted with a Fujinon 1/2" 6mm lens (DF6HA-1B). A high transmittance (approximately 98%) Tiffen 72mm linear polarization filter was placed in front of the lens, using a mounted protractor having 2° increments. Both camera and filter were rigidly connected to a rotating stage, having its own protractor. In this section, we held the stage static and rotated only the filter. This way, we performed traditional polarimetric imaging, yielding ground truth $c(\boldsymbol{x}_{\text{obj}})$, $p(\boldsymbol{x}_{\text{obj}})$, and $\theta(\boldsymbol{x}_{\text{obj}})$. Pixels having saturated intensity were noted, in order to be ignored in the subsequent estimation of ω. The scene's polarization field is visualised in Fig. 5. The visualization[1] is based on the hue-saturation-value (HSV) color space.

[1] The maps of each polarization variable are presented in the *Supplementary Material*.

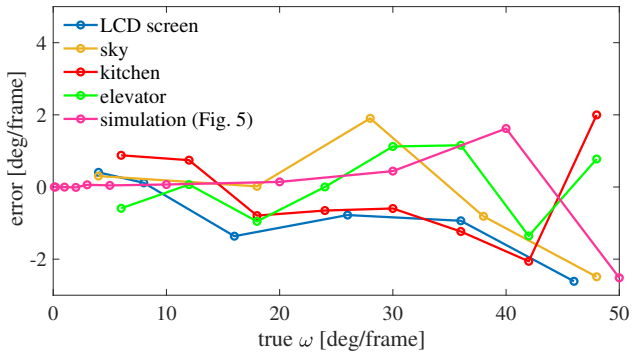

Fig. 6. Plots of error(ω) for the simulated tests and real experiments.

The value channel represents the monochrome $c(\boldsymbol{x}_{\rm obj})$. The hue and saturation channels represent, respectively, the AOP $\theta(\boldsymbol{x}_{\rm obj})$ and the DOP $p(\boldsymbol{x}_{\rm obj})$.

Using the scene polarization, $c(\boldsymbol{x}_{\rm obj}), p(\boldsymbol{x}_{\rm obj})$ and $\theta(\boldsymbol{x}_{\rm obj})$, we simulated two acquired frames $I(\boldsymbol{x}_{\rm cam}, 1), I(\boldsymbol{x}_{\rm cam}, 2)$, where a simulated polarization filter was rigidly attached to the camera. Between these frames, the simulated camera+filter rig was rigidly rotated by $\omega\Delta t$ of our choosing. We define $\Delta t = 1$[frame]. Then, we introduced Poisson (photon) noise to the images, using a scale of 50 photo-electrons per 8-bit graylevel.

In analysis, images were slightly smoothed by a Gaussian filter (STD of 2 pixels). The weight in Eq. (26) was set $\mu = 0.0001$. Ten tests were carried out, each with a different rotation $\omega \in [0.1^\circ/\text{frame}, \dots\ 50^\circ/\text{frame}]$. Each test yielded an estimate of ω. To assess uncertainty, this process was repeated 10 times, using independent Poisson noise samples. Using these samples, per tested rotation angle we obtained an average estimate $\hat{\bar{\omega}}$ and standard deviation STD($\hat{\omega}$). We found that typically STD($\hat{\omega}$) $\approx 0.03^\circ$/frame. The resulting error(ω) $\equiv \hat{\bar{\omega}} - \omega$ is plotted in Fig. 6. The approach performed well across a wide range of angles.

9 Experiments

The experiments use the system described in Sec. 8 and Fig. 4. Here, however, the polarizer protractor was held fixed relative to the camera. The rotating stage that held the camera+polarizer rig was rotated relative to the scene. Only two frames are taken per experiment, each angle in the pair is fixed and known. Rotation between angles is done manually, then a shot is taken. This is in lieu of having two images sampled automatically in a motorized rig. We captured four scenes: *LCD*, *Kitchen*, *Sky*, and *Elevator*. They are visualized in Fig. 7 and described below. Each scene lead to 5-8 experiments, each at a distinct rotation rate $\omega \in [4^\circ/\text{frame}, \dots\ 48^\circ/\text{frame}]$. This yielded a total of 27 experiments. The resulting error(ω) $= \hat{\bar{\omega}} - \omega$ is plotted in Fig. 6. The approach performed well across a wide range of angles.

Fig. 7. *LCD screen*, *Kitchen*, *Sky*, and *Elevator* scenes. The polarization is represented using the HSV color space, as in Fig. 5.

• *LCD screen* is simply a computer screen displaying a photo. Its spatial contrast in c is strong. Its DOP is nearly $p = 1$. Slight depolarization is caused by unpolarized light in the lab reflecting off the screen.
• *Kitchen* possesses reflection-induced polarization at a variety of angles. Light thus has a variety of polarization angles. The DOP is generally low. This scene has a lot of intensity edges.
• *Elevator* presents a low light, high DOP scene, with a weak pattern of a rough reflecting metallic surface.
• In *Sky*, the rig views the clear sky through the lab's open window. The viewed sky is highly polarized ($p \approx 0.6$), having nearly uniform radiance. Such a scene can be challenging for traditional image-based ego-rotation estimation.

We imaged a sky-patch using $\omega = 6°$/frame. Our method erred by 5%. We imaged this sky patch in the same rotation setting, without a polarizer. We ran Horn-Schunck and Lucas-Kanade optical-flow algorithms on the radiance measurements. The resulting flows were fit by least-squares to rotation, yielding respectively, $\hat{\omega} = 0.1°$/frame and $\hat{\omega} = 0.03°$/frame, i.e., far lower than ω.

To compare with [29,30], we imaged Stokes vector per pixel of the sky patch, by rotating the polarizer independently of the camera, and then rotating the camera itself. We then ran the Horn-Schunck and Lucas-Kanade algorithms on the DOP field p, as in [29, 30]. Using the resulting flow fields for least-squares fit to rotation yielded, respectively, $\hat{\omega} = 10^{-5}$ °/frame and $2 \cdot 10^{-5}$ °/frame. These estimated values are far lower than the true $\omega = 6°$/frame. The spatial uniformity of the radiance and DOP fields yield no reliable information about rotation. The sky's AOP enables proper estimation of rotation.

10 Conclusions

The *polarized optical-flow equation* (12) contains both traditional components of optical-flow and a polarized component. In strong spatial gradients of radiance, flow estimation is similar to optical-flow, while polarization is just an enhancement. In weak spatial gradient, or when spatial resolution is low (low resource sensors) the polarized component may have similar and even higher significance than the optical-flow. The approach can be useful in low-resource

outdoor navigation having the sky in view or underwater. Polarization-based navigation aids [17, 18, 19, 21, 67, 79] fit low resource systems, but they assume models of the expected polarization pattern. This paper shows that the rotation rate can be derived in unknown scenes. In addition, this rotation cue can assist self-calibration of distant imagers, such as low-resource nano-satellites [61].

The optical-flow model assumes infinitesimal motion. Nevertheless, the estimation results here were found to be reasonable even in rather large angles of rotation. It is worth generalizing analysis for motion having arbitrarily large angles and more complex parametric ego-motion, including translation and 3-axis rotation. We believe that a 3-axis rotation sensor can be achieved by having a rig containing three corresponding cameras, each having a mounted polarizer. Alternatively, this may be achieved using an omnicam mounted with a polarizer having a spatially varying polarization axis [6, 60].

There are sensors in which micro-polarizers are attached to individual pixels [1, 25]. Adjacent pixels use filters that are 45° or 90° to each other, in analogy to RGB Beyer patterns. It is worth extending the analysis to such cameras. There, a single image yields $\hat{\mathbf{\Gamma}}$, thus significantly simplifying the analysis of Sec. 7.

The work here may shed light on biology. As described in Sec. 2, many animals use a polarization compass. However, many animals have eyes that are both spatially resolving and polarization sensitive. It is common for their eyes to have two interleaved populations of receptor cells, having mutually orthogonal orientations [38]. It is possible to study whether these animals combine these principles, in analogy to our analysis.

We use a particular algorithm for recovery, and as most algorithms, it has pros, cons and parameters. For example, in our implementation, we use an initial optimization step-size which decreases when ω increases. We believe that algorithms that are designed to be efficient and robust in low resource systems would suit the sensing idea of this paper.

11 Acknowledgements

We thank M. Sheinin, A. Levis, A. Vainiger, T. Loeub, V. Holodovsky, M. Fisher, Y. Gat, and O. Elezra for fruitful discussions. We thank I. Czerninski, O. Shubi, D. Yegudin, and I. Talmon for technical support. Yoav Schechner is the Mark and Diane Seiden Chair in Science at the Technion. He is a Landau Fellow - supported by the Taub Foundation. His work was conducted in the Ollendorff Minerva Center. Minvera is funded through the BMBF. This work is supported by the Israel Science Foundation (ISF fund 542/16).

References

1. Technology Image Sensor: Polarization Products Sony Semiconductor Solutions Group, `https://www.sony-semicon.co.jp/e/products/IS/polarization/technology.html`, accessed 2020-07-16

2. Agrawal, P., Ratnoo, A., Ghose, D.: Inverse optical flow based guidance for UAV navigation through urban canyons. Aerospace Science and Technology **68**, 163–178 (2017)
3. Barta, A., Horváth, G.: Underwater binocular imaging of aerial objects versus the position of eyes relative to the flat water surface. JOSA A **20**(12), 2370 (2003)
4. Ben-Ezra, M.: Segmentation with invisible keying signal. In: CVPR. pp. 32–37. IEEE (2000)
5. Berezhnyy, I., Dogariu, A.: Time-resolved Mueller matrix imaging polarimetry. Optics Express **12**(19), 4635–4649 (2004)
6. Bomzon, Z., Biener, G., Kleiner, V., Hasman, E.: Spatial fourier-transform polarimetry using space-variant subwavelength metal-stripe polarizers. Optics Letters **26**(21), 1711–1713 (2001)
7. Brines, M.L.: Dynamic patterns of skylight polarization as clock and compass. Journal of Theoretical Biology **86**(3), 507–512 (1980)
8. Brines, M.L., Gould, J.L.: Skylight Polarization patterns and Animal Orientation. Journal of Experimental Biology **96**(1), 69–91 (1982)
9. Carey, S.J., Barr, D.R., Dudek, P.: Low power high-performance smart camera system based on SCAMP vision sensor. Journal of Systems Architecture **59**(10), 889–899 (2013)
10. Chahl, J.S., Srinivasan, M.V., Zhang, S.W.: Landing strategies in honeybees and applications to uninhabited airborne vehicles. The International Journal of Robotics Research **23**(2), 101–110 (2004)
11. Collin, C., Pattanaik, S., LiKamWa, P., Bouatouch, K.: Computation of polarized subsurface BRDF for rendering. In: Proceedings of Graphics Interface. pp. 201–208. Canadian Information Processing Society (2014)
12. Courroux, S., Chevobbe, S., Darouich, M., Paindavoine, M.: Use of wavelet for image processing in smart cameras with low hardware resources. Journal of Systems Architecture **59**(10), 826–832 (2013)
13. Cronin, T.W.: Polarization vision and its role in biological signaling. Integrative and Comparative Biology **43**(4), 549–558 (2003)
14. Dahlberg, A.R., Pust, N.J., Shaw, J.A.: Effects of surface reflectance on skylight polarization measurements at the Mauna Loa Observatory. Optics Express **19**(17), 16008–16021 (2011)
15. Diamant, Y., Schechner, Y.Y.: Overcoming visual reverberations. In: CVPR. pp. 1–8. IEEE (2008)
16. Diner, D.J., Davis, A., Hancock, B., Geier, S., Rheingans, B., Jovanovic, V., Bull, M., Rider, D.M., Chipman, R.A., Mahler, A.B., et al.: First results from a dual photoelastic-modulator-based polarimetric camera. Applied Optics **49**(15), 2929–2946 (2010)
17. Dupeyroux, J., Diperi, J., Boyron, M., Viollet, S., Serres, J.: A novel insect-inspired optical compass sensor for a hexapod walking robot. In: IROS. pp. 3439–3445. IEEE/RSJ (2017)
18. Dupeyroux, J., Serres, J., Viollet, S.: A hexapod walking robot mimicking navigation strategies of desert ants cataglyphis. In: Living Machines: Conference on Biomimetic and Biohybrid Systems. pp. 145–156. Springer (2018)
19. Dupeyroux, J., Viollet, S., Serres, J.R.: An ant-inspired celestial compass applied to autonomous outdoor robot navigation. Robotics and Autonomous Systems **117**, 40–56 (2019)
20. Evangelista, C., Kraft, P., Dacke, M., Labhart, T., Srinivasan, M.: Honeybee navigation: Critically examining the role of the polarization compass. Philosophical

Transactions of the Royal Society B: Biological Sciences **369**(1636), 20130037 (2014)
21. Fan, C., Hu, X., Lian, J., Zhang, L., He, X.: Design and calibration of a novel camera-based bio-inspired polarization navigation sensor. IEEE Sensors Journal **16**(10), 3640–3648 (2016)
22. Farid, H., Adelson, E.H.: Separating reflections from images by use of independent component analysis. JOSA A **16**(9), 2136–2145 (1999)
23. Fernandes, J., Postula, A., Srinivasan, M., Thurrowgood, S.: Insect inspired vision for micro aerial vehicle navigation. In: ACRA. pp. 1–8. ARAA (2011)
24. Foster, J.J., Sharkey, C.R., Gaworska, A.V., Roberts, N.W., Whitney, H.M., Partridge, J.C.: Bumblebees learn polarization patterns. Current Biology **24**(12), 1415–1420 (2014)
25. Garcia, M., Edmiston, C., Marinov, R., Vail, A., Gruev, V.: Bio-inspired color-polarization imager for real-time in situ imaging. Optica **4**(10), 1263 (2017)
26. Gill, P.R., Kellam, M., Tringali, J., Vogelsang, T., Erickson, E., Stork, D.G.: Computational diffractive imager with low-power image change detection. In: Computational Optical Sensing and Imaging. pp. CM3E–2. OSA (2015)
27. Goddard, S.M., Forward, R.B.: The role of the underwater polarized light pattern, in sun compass navigation of the grass shrimp, Palaemonetes Vulgaris. Journal of Comparative Physiology A: Neuroethology, Sensory, Neural, and Behavioral Physiology **169**(4), 479–491 (1991)
28. Gruev, V., Van der Spiegel, J., Engheta, N.: Dual-tier thin film polymer polarization imaging sensor. Optics Express **18**(18), 19292–19303 (2010)
29. Guan, L., Liu, S., qi Li, S., Lin, W., yuan Zhai, L., kui Chu, J.: Study on polarized optical flow algorithm for imaging bionic polarization navigation micro sensor. Optoelectronics Letters **14**(3), 220–225 (2018)
30. Guan, L., Zhai, L., Cai, H., Zhang, P., Li, Y., Chu, J., Jin, R., Xie, H.: Study on displacement estimation in low illumination environment through polarized contrast-enhanced optical flow method for polarization navigation applications. Optik **210**, 164513 (2020)
31. Guarnera, G.C., Peers, P., Debevec, P., Ghosh, A.: Estimating surface normals from spherical Stokes reflectance fields. In: ECCV. pp. 340–349. Springer (2012)
32. Guo, Q., Shi, Z., Huang, Y.W., Alexander, E., Qiu, C.W., Capasso, F., Zickler, T.: Compact single-shot metalens depth sensors inspired by eyes of jumping spiders. Proceedings of the National Academy of Sciences **116**(46), 22959–22965 (2019)
33. Gupta, M., Narasimhan, S.G., Schechner, Y.Y.: On controlling light transport in poor visibility environments. In: CVPR. pp. 1–8. IEEE (2008)
34. Gutierrez, D., Narasimhan, S.G., Jensen, H.W., Jarosz, W.: Scattering. In: ACM Siggraph Asia Courses. p. 18 (2008)
35. Hooper, B.A., Baxter, B., Piotrowski, C., Williams, J., Dugan, J.: An airborne imaging multispectral polarimeter. In: Oceans. vol. 2, p. 7. IEEE/MTS (2009)
36. Horisaki, R., Choi, K., Hahn, J., Tanida, J., Brady, D.J.: Generalized sampling using a compound-eye imaging system for multi-dimensional object acquisition. Optics Express **18**(18), 19367–19378 (2010)
37. Horstmeyer, R., Euliss, G., Athale, R., Levoy, M.: Flexible multimodal camera using a light field architecture. In: ICCP. pp. 1–8. IEEE (2009)
38. Horváth, G.: Polarized light and polarization vision in animal sciences, vol. 2. Springer (2014)
39. Ihrke, I., Kutulakos, K.N., Lensch, H.P., Magnor, M., Heidrich, W.: State of the art in transparent and specular object reconstruction. In: Eurographics STAR - state of the art report (2008)

40. Joos, F., Buenzli, E., Schmid, H.M., Thalmann, C.: Reduction of polarimetric data using Mueller calculus applied to Nasmyth instruments. In: Observatory Operations: Strategies, Processes, and Systems II. vol. 7016, p. 70161I. SPIE (2008)
41. Kadambi, A., Taamazyan, V., Shi, B., Raskar, R.: Polarized 3d: High-quality depth sensing with polarization cues. In: ICCV. pp. 3370–3378. IEEE (2015)
42. Kadambi, A., Taamazyan, V., Shi, B., Raskar, R.: Depth sensing using geometrically constrained polarization normals. International Journal of Computer Vision **125**(1-3), 34–51 (2017)
43. Kaftory, R., Schechner, Y.Y., Zeevi, Y.Y.: Variational distance-dependent image restoration. In: CVPR. pp. 1–8. IEEE (2007)
44. Kattawar, G.W., Adams, C.N.: Stokes vector calculations of the submarine light field in an atmosphere-ocean with scattering according to a Rayleigh phase matrix: Effect of interface refractive index on radiance and polarization. Limnology and Oceanography **34**(8), 1453–1472 (1989)
45. Kong, N., Tai, Y.W., Shin, J.S.: A physically-based approach to reflection separation: from physical modeling to constrained optimization. IEEE Transactions on Pattern Analysis and Machine Intelligence **36**(2), 209–221 (2013)
46. Lanman, D., Wetzstein, G., Hirsch, M., Heidrich, W., Raskar, R.: Polarization fields: dynamic light field display using multi-layer LCDs. In: ACM Transactions on Graphics. vol. 30, p. 186 (2011)
47. Lerner, A., Sabbah, S., Erlick, C., Shashar, N.: Navigation by light polarization in clear and turbid waters. Philosophical Transactions of the Royal Society B: Biological Sciences **366**(1565), 671–679 (2011)
48. Levis, A., Schechner, Y.Y., Davis, A.B., Loveridge, J.: Multi-view polarimetric scattering cloud tomography and retrieval of droplet size. arXiv preprint arXiv:2005.11423 (2020)
49. Maeda, T., Kadambi, A., Schechner, Y.Y., Raskar, R.: Dynamic heterodyne interferometry. In: ICCP. pp. 1–11. IEEE (2018)
50. McGuire, K., De Croon, G., De Wagter, C., Tuyls, K., Kappen, H.: Efficient optical flow and stereo vision for velocity estimation and obstacle avoidance on an autonomous pocket drone. IEEE Robotics and Automation Letters **2**(2), 1070–1076 (2017)
51. Miyazaki, D., Saito, M., Sato, Y., Ikeuchi, K.: Determining surface orientations of transparent objects based on polarization degrees in visible and infrared wavelengths. JOSA A **19**(4), 687–694 (2002)
52. Mohan, A., Woo, G., Hiura, S., Smithwick, Q., Raskar, R.: Bokode: imperceptible visual tags for camera based interaction from a distance. In: ACM Transactions on Graphics. vol. 28, p. 98 (2009)
53. Monjur, M., Spinoulas, L., Gill, P.R., Stork, D.G.: Panchromatic diffraction gratings for miniature computationally efficient visual-bar-position sensing. Sensors & Transducers **194**(11), 127 (2015)
54. Mujat, M., Baleine, E., Dogariu, A.: Interferometric imaging polarimeter. JOSA A **21**(11), 2244–2249 (2004)
55. Pijnacker Hordijk, B.J., Scheper, K.Y., De Croon, G.C.: Vertical landing for micro air vehicles using event-based optical-flow. Journal of Field Robotics **35**(1), 69–90 (2018)
56. Reddy, D., Veeraraghavan, A., Chellappa, R.: P2C2: Programmable pixel compressive camera for high speed imaging. In: CVPR. pp. 329–336. IEEE (2011)
57. Schechner, Y.Y.: Inversion by P4: polarization-picture post-processing. Philosophical Transactions of the Royal Society B: Biological Sciences **366**(1565), 638–648 (2011)

58. Schechner, Y.Y.: Self-calibrating imaging polarimetry. In: ICCP. pp. 1–10. IEEE (2015)
59. Schechner, Y.Y., Diner, D.J., Martonchik, J.V.: Spaceborne underwater imaging. In: ICCP. pp. 1–8. IEEE (2011)
60. Schechner, Y.Y., Nayar, S.K.: Generalized mosaicing: Polarization panorama. IEEE Transactions on Pattern Analysis and Machine Intelligence **27**(4), 631–636 (2005)
61. Schilling, K., Schechner, Y., Koren, I.: Cloudct-computed tomography of clouds by a small satellite formation. In: Proceedings of the 12th IAA symposium on Small Satellites for Earth Observation (2019)
62. Shantaiya, S., Verma, K., Mehta, K.: Multiple object tracking using Kalman filter and optical flow. European Journal of Advances in Engineering and Technology **2**(2), 34–39 (2015)
63. Shashar, N.: Transmission of linearly polarized light in seawater: implications for polarization signaling. Journal of Experimental Biology **207**(20), 3619–3628 (2004)
64. Shashar, N., Johnsen, S., Lerner, A., Sabbah, S., Chiao, C.C., Mathger, L.M., Hanlon, R.T.: Underwater linear polarization: physical limitations to biological functions. Philosophical Transactions of the Royal Society B: Biological Sciences **366**(1565), 649–654 (2011)
65. Shashar, N., Rutledge, P., Cronin, T.: Polarization vision in cuttlefish in a concealed communication channel? The Journal of Experimental Biology **199**(9), 2077–84 (1996)
66. Shashar, N., Hagan, R., Boal, J.G., Hanlon, R.T.: Cuttlefish use polarization sensitivity in predation on silvery fish. Vision Research (2000)
67. Shashar, N., Milbury, C., Hanlon, R.: Polarization vision in Cephalopods: Neuroanatomical and behavioral features that illustrate aspects of form and function. Marine and Freshwater Behaviour and Physiology (2002)
68. Shen, C., Bai, Z., Cao, H., Xu, K., Wang, C., Zhang, H., Wang, D., Tang, J., Liu, J.: Optical flow sensor/INS/magnetometer integrated navigation system for MAV in GPS-denied environment. Journal of Sensors **2016** (2016)
69. Smith, F., Stewart, D.: Robot and insect navigation by polarized skylight. In: Biosignals. pp. 183–188 (2014)
70. Song, X., Seneviratne, L.D., Althoefer, K.: A Kalman filter-integrated optical flow method for velocity sensing of mobile robots. IEEE/ASME Transactions on Mechatronics **16**(3), 551–563 (2010)
71. Srinivasan, M.V.: Honeybees as a model for the study of visually guided flight, navigation, and biologically inspired robotics. Physiological Reviews **91**(2), 413–460 (2011)
72. Stork, D.G.: Optical elements as computational devices for low-power sensing and imaging. In: Imaging Systems and Applications. pp. ITu4E–4. OSA (2017)
73. Stork, D.G., Gill, P.R.: Special-purpose optics to reduce power dissipation in computational sensing and imaging systems. In: Sensors. pp. 1–3. IEEE (2017)
74. Tanaka, K., Mukaigawa, Y., Matsushita, Y., Yagi, Y.: Descattering of transmissive observation using parallel high-frequency illumination. In: ICCP. pp. 1–8. IEEE (2013)
75. Tessens, L., Morbée, M., Philips, W., Kleihorst, R., Aghajan, H.: Efficient approximate foreground detection for low-resource devices. In: International Conference on Distributed Smart Cameras. pp. 1–8. ACM/IEEE (2009)
76. Thurrowgood, S., Moore, R.J., Soccol, D., Knight, M., Srinivasan, M.V.: A biologically inspired, vision-based guidance system for automatic landing of a fixed-wing aircraft. Journal of Field Robotics **31**(4), 699–727 (2014)

77. Treeaporn, V., Ashok, A., Neifeld, M.A.: Increased field of view through optical multiplexing. Optics Express **18**(21), 22432–22445 (2010)
78. Treibitz, T., Schechner, Y.Y.: Polarization: Beneficial for visibility enhancement? In: CVPR. pp. 525–532. IEEE (2009)
79. Tyo, J.S., Goldstein, D.L., Chenault, D.B., Shaw, J.A.: Review of passive imaging polarimetry for remote sensing applications. Applied Optics **45**(22), 5453–5469 (2006)
80. Umeyama, S., Godin, G.: Separation of diffuse and specular components of surface reflection by use of polarization and statistical analysis of images. IEEE Transactions on Pattern Analysis and Machine Intelligence (5), 639–647 (2004)
81. Wang, D., Liang, H., Zhu, H., Zhang, S.: A bionic camera-based polarization navigation sensor. Sensors **14**(7), 13006–13023 (2014)
82. Wehner, R.d.: Polarized-light navigation by insects. Scientific American **235**(1), 106–115 (1976)
83. Xu, Z., Yue, D.K., Shen, L., Voss, K.J.: Patterns and statistics of in-water polarization under conditions of linear and nonlinear ocean surface waves. Journal of Geophysical Research: Oceans **116**(12), 1–14 (2011)
84. Yuan, W., Dana, K., Varga, M., Ashok, A., Gruteser, M., Mandayam, N.: Computer vision methods for visual MIMO optical system. In: CVPR Workshops. pp. 37–43. IEEE (2011)
85. Zallat, J., Torzynski, M., Lallement, A.: Double-pass self-spectral-calibration of a polarization state analyzer. Optics Letters **37**(3), 401–403 (2012)
86. Zhang, L., Hancock, E.R., Atkinson, G.A.: Reflection component separation using statistical analysis and polarisation. In: Iberian Conference on Pattern Recognition and Image Analysis. pp. 476–483 (2011)